Internal relaxation time in immersed particulate materials

P. Rognon and I. Einav*
School of Civil Engineering, J05, The University of Sydney, Sydney, New South Wales 2006, Australia

C. Gay†
Matière et Systèmes Complexes, Université Paris Diderot–Paris 7, CNRS, UMR 7057, Bâtiment Condorcet, Case Courrier 7056, F-75205 Paris Cedex 13, France

(Received 3 August 2009; revised manuscript received 31 March 2010; published 23 June 2010)

We study the dynamics of the static-to-flow transition in a model material made of elastic particles immersed in a viscous fluid. The interaction between particle surfaces includes their viscous lubrication, a sharp repulsion when they get closer than a tuned steric length, and their elastic deflection induced by those two forces. We use soft dynamics to simulate the dynamics of this material when it experiences a step increase in the shear stress and a constant normal stress. We observe a long creep phase before a substantial flow eventually establishes. We measure the change in volume (dilatancy) and find that during the creep phase, it does not change significantly. We find that the typical creep time relies on an internal relaxation process, namely, the separation of two particles driven by the applied stress and resisted by the viscous friction. The present mechanism should be relevant for granular pastes, living cells, emulsions, and wet foams.

DOI: 10.1103/PhysRevE.81.061304 PACS number(s): 45.70.−n, 82.70.−y, 83.80.Iz, 02.70.Ns

I. INTRODUCTION

The rheological behavior of soft amorphous materials such as foams [1,2], emulsions [3–5], living cells [6], and granular pastes [7,8] is an active field of research with many practical issues, for these materials are broadly involved in geophysical events, industrial processes, and biological organisms. Besides, understanding their dynamics presents great theoretical challenges as their structure, similar to that of glasses, is disordered, metastable, and out of thermodynamical equilibrium [9,10].

Perhaps the most salient property of these materials is their ability to deform like a solid or to flow like a liquid depending on the loading conditions. At the microscopic level, this static-to-flow transition relies on the particles ability to move with respect to each other, similar to the cage effect in molecular or colloidal systems [11,12]. However, large enough bubbles, droplets and grains do not show significant Brownian motion and this transition is thus not thermally activated. The *driving force* of the relative particle motion comes only from the external loading, while the *resisting force* comes from the particle interactions and/or deformations. This force balance defines internal dynamics with an associated time scale, which is the core of the thixotropy effects in various materials [12–16] and of the relaxation time evidenced by oscillatory shear experiments [17,18]. The interstitial liquid is pivotal to these internal dynamics, as it affects both the *driving force* and the *resisting force* experienced by the particles.

Immersed particulate materials support the stresses not only through their contact network (known as osmotic or effective stresses) but also by the continuous liquid (pore pressure). This notion of pore pressure is a central point of soil stability analysis (see [19] and reference therein) and was shown to be responsible for a long delay in the triggering of submarine granular avalanches [20]. The underlying mechanism involves the dilatancy needed to start shearing and the time required to fill the growing pores with liquid. This filling time then relies on the degree of drainage of the shearing zone, in other words on how long the liquid takes to flow from one part of the material to another. Assuming that the granular skeleton does not deform, the flow of liquid through the pore network satisfies a Darcy law with some permeability depending on the solid fraction [20]. Experiments with foams have also revealed the importance of the permeation through the pore network on the time required to increase the liquid fraction during the development of shear bands [21].

Beside its role for pore pressure, the liquid can strongly affect the short-range particle interactions as it lubricates close pairs of surfaces. This interaction is well known for smooth rigid and spherical particles (see, for instance, [22]). A discrete element method, named "Stokesian dynamics," has been developed and broadly used to simulate the dynamics of individual particles in suspensions undergoing both long-range multibody hydrodynamic interactions and short-range lubrication between rigid surfaces [23–26]. We showed in previous works that, when the particles get very close, the elastic (Hertzian) deformation of their surfaces induced by the viscous forces cannot be neglected, as it strongly affects the geometry of the lubricated flow and the associated viscous friction [27,28]. We highlighted that each surface deflection is then not directly given by the particle positions but results from its own force and torque balances. We therefore introduced a new discrete element method, named *soft dynamics*, which simulates such surface dynamics beside those of the particles centers.

In this paper, we use the soft dynamics to investigate the dynamics of a suspension of elastic and smooth spheres which undergoes a static-to-flow transition. From a static compressed state, we subject the sample to a smoothed step-

*itai.einav@sydney.edu.au
†cyprien.gay@univ-paris-diderot.fr

wise increase in the shear stress while the normal stress is kept constant and measure the delay before the onset of a steady flow. We show that this macroscopic delay reflects the dynamics of a simple internal process: the separation of two grains driven by a tensile force that results from the applied stress and resisted by the normal viscous friction. The material under consideration corresponds to an ideal suspension, whose grains is purely elastic and interacts only by lubricated contacts with a steric repulsion when surfaces get very close. In real immersed materials, others mode of interaction interplay with the lubrication flow, which can lead to different dynamics of separation and even to new dominant relaxation processes. One can cite, for instance: the asperities on rough solid surfaces [29–32], the viscoelastic stretching of the interfaces of bubbles or droplets [33,34], their permeability [35], their electrostatic repulsion which leads to disjuncting pressure [36], as well as adhesion [2,37,38]. The analysis developed in this paper through the soft dynamics method could characterize other macroscopic behavior of these dense immersed particulate materials, such as thixotropy, by adapting the leading mode of interaction controlled by their own dynamics.

II. INTERNAL DYNAMICS: INSIGHTS FROM DIMENSIONAL ANALYSIS

Dimensional analysis is often used to define the typical basic times that the system involves. Let us recall its outcome, as expressed in various studies. We are dealing with elastic particles of size d, the Young's modulus E, and mass m. They are immersed in a Newtonian fluid (viscosity η) and confined by an osmotic normal stress σ_{yy}. Four time scales emerge from those quantities.

The first two time scales correspond to the motion of a single particle which experiences a driving force $\sigma_{yy}d^2$. For dry grains, this motion is resisted only by the grain inertia (mass m), while for particles with negligible mass immersed in a fluid of viscosity η, it is resisted merely by the Stokes drag. The respective corresponding times are the *inertial time* t_i [39–41] and the *Stokes time* t_{St} [42–44]:

$$t_i = \sqrt{\frac{m}{\sigma_{yy}d}}, \tag{1}$$

$$t_{St} = 3\pi\frac{\eta}{\sigma_{yy}}. \tag{2}$$

The other two time scales can be directly obtained by replacing the scale of stress σ_{yy} by the Young's modulus E in each above time scale. This leads to the time t_c for sound to propagate through a grain (which can also be linked to the binary collision time [45]) and to the time t_M for an elastically deformed particle to recover its shape when immersed in a viscous fluid, a time similar to that of a Maxwell relaxation [46,47]:

$$t_c = \sqrt{\frac{m}{Ed}}, \tag{3}$$

TABLE I. Order of magnitudes of the internal time scales in immersed particulate systems. Time scales from dimensional analysis (defined in Sec. II) and delay time scale Δ from lubrication interactions (computed through the present paper). Particles consist in grains or bubbles of size $d=1$ mm immersed in water (viscosity 10^{-3} Pa s). The grain density is 2×10^3 kg m^{-3} and their Young modulus is 10^{10} Pa. The density of bubbles is null and their effective Young modulus is of the order of $E\approx10^2$ Pa. We consider an osmotic normal stress of 10^7 Pa for the grains and 10^{-1} Pa for the bubbles in order to obtain the same reduced normal stress $\kappa=\sigma_{yy}/E=10^{-3}$ in both cases. The delay Δ is estimated according to Eq. (8) with a steric length of $h_0=10^{-7}$ m, which corresponds to particles in the Hertz limit.

Time (s)	t_i	t_{St}	t_c	t_M	Δ
Grains	10^{-5}	10^{-9}	$10^{-7.5}$	10^{-13}	$10^4 t_{St}$
Bubbles	0	10^{-1}	0	10^{-5}	$10^4 t_{St}$ [a]

[a]The above delay Δ was based on Hertzian elasticity. Of course, bubbles and droplets do not display any bulk elasticity, yet they do recover their shape upon load reversal. For the present purpose, their effective Young's modulus was estimated as the surface tension (10^{-1} N m^{-1}) divided by the bubble size: $E\approx10^2$ Pa (see [33] for more details on droplet contact).

$$t_M = \frac{\eta}{E}. \tag{4}$$

Table I gives an estimate of those time scales for elastic grains and for bubbles. For the particle deformation to remain moderate, the reduced normal stress $\kappa=\frac{\sigma_{yy}}{E}$ must be small, and time scale t_c (respectively, t_M) is thus shorter than t_i (respectively, t_{St}).

The above references clearly show the usefulness of such time scales, especially for expressing flow laws. However, none of them accounts for the details of the interaction of a particle with its neighborhood. The aim of the present paper is to point out the importance of such a time scale when particles are elastic and interact via lubricated contacts.

III. INTERNAL DYNAMICS: PARTICLE INTERACTION

We consider an ideal suspension made of elastic particles in a Newtonian fluid. We focus on dense configurations, where the surface-to-surface distance h between a particle and its few closest neighbors is typically much smaller than the particle diameter d. Under such conditions, the particle-fluid-particle interaction is mostly governed by the liquid that is present within a small gap of thickness h and radius a with $h \ll a \ll d$ [Fig. 1(a)]. Accordingly, the force and torque transmitted from surface to surface within each pair of neighboring particles are proportional to their relative velocity. For such a gap with a low aspect ratio ($h \ll a$) in which the flow satisfies the conditions of the lubrication approximation, the proportionality coefficients (which we here call viscous frictions) can be expressed rather easily (see Appendix A) as functions of the gap thickness h and size a.

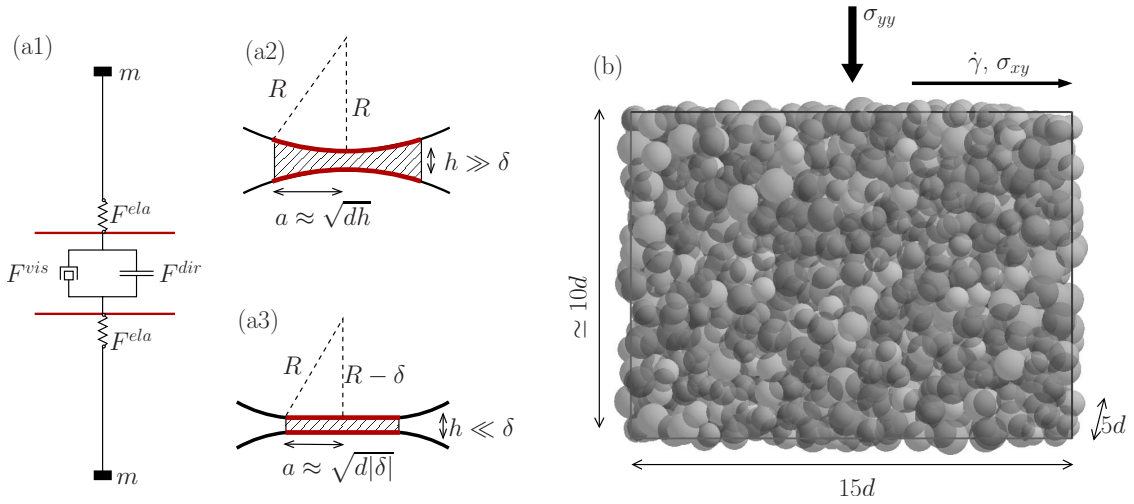

FIG. 1. (Color online) (a) Particle-fluid-particle interaction: (a1) the force F^{ela} that deforms the surface elastically decomposes into the viscous force F^{vis} and the direct particle-particle force F^{dir}. The size a of the transmitting force region is represented in two asymptotic limits: (a2) the Poiseuille limit for nondeflecting spheres and (a3) the Hertz limit when the deflection δ is much larger than the gap width h. (b) Plane shear simulated using soft dynamics. 1000 particles are subjected to normal stress σ_{yy} and shear stress σ_{xy} in a periodic domain (Lees-Edwards boundary conditions [48]). The height of the cell fluctuates freely in order to keep σ_{yy} constant.

As a result of the viscous force and torque transmitted through the gap, the particle surfaces locally deform elastically. Hence, for each pair of close neighbors, the combination of the gap viscous response and the particle elasticities is analogous to a Maxwell element [see Fig. 1a1] in which both the stiffness and the viscous friction are nonlinear (in the sense that they depend on the gap geometry) and tensorial (since they reflect the normal, tangential, and twist modes, see Fig. 7).

The viscous friction term that represents the normal relative motion (Poiseuille flow) turns out to be typically much higher than the corresponding terms for the tangential sliding mode (Couette flow) and the twist mode. Thus, the normal relative motion should be responsible for the longest relaxation time. Let us therefore recall the expression of the normal viscous and elastic forces (see Appendix A):

$$F_n^{vis} = \frac{3}{2}\pi\eta\frac{a^4}{h^3}\dot{h}, \tag{5}$$

$$F_n^{ela} = aE\delta, \tag{6}$$

where E is the Young's modulus of the particle and δ is the normal surface deflection. The size a of the region that transmits most of the force basically depends on the distance between surfaces and on the flattening induced by their elastic deflections. If the elastic deflection is much smaller than the gap thickness, the surface shape is mostly spherical and the size a is given by the classical lubrication approximation between two spheres: $a \approx \sqrt{dh}$ [Fig. 1a2]. We refer to this asymptotic limit as the *Poiseuille* limit. Conversely, if the elastic deflection is much larger than the gap thickness, the particle surface elastically flattens over a region whose size is given by Hertz's theory: $a \approx \sqrt{d\delta}$ [Fig. 1a3]. We refer to this asymptotic limit as the *Hertz* limit.

So far, two particles could not statically sustain any nonzero confining force since the fluid would keep flowing out of the gap and the particle surfaces would correspondingly keep approaching although in a slower and slower motion. In practice, however, there is usually a typical distance h_0 below which particle surfaces interact not only via the fluid but also through a direct particle-particle force. This interaction can have various physical origins, among which direct contacts between asperities of rough solid surfaces [29–32] or repulsion between charged or polymeric surfactant molecules at the bubble or droplet surface [36]. Our present focus is not necessarily to capture any of the details of such effects but rather to represent their common feature: a strong steric repulsion that works on the particle surfaces in parallel to the viscous force [Fig. 1a1]. For that purpose, we chose the following power law:

$$F_n^{dir} = F_n^{conf}\left(\frac{h}{h_0}\right)^{-\alpha}. \tag{7}$$

For $\alpha \gg 1$, this law captures our requirement for a strongly increasing repulsion as the gap becomes thinner than the steric length h_0 and a quickly vanishing repulsion for thicker gaps. Ideally, we would have liked to have an infinite α, but as this function becomes more strongly nonlinear, the critical time step for accurate simulations increases tremendously. A value of $\alpha=8$ was found as a good compromise between these two requirements. The force scale parameter is chosen as $F_n^{conf}=\sigma_{yy}d^2$. In this way, the surface-to-surface distances stabilize around h_0 when the material is subjected to a confining stress σ_{yy}.

IV. COLLECTIVE RESPONSE TO A STEP SHEAR STRESS

In this section, we use soft dynamics to study the response of the material to a sudden increase in shear stress in plane

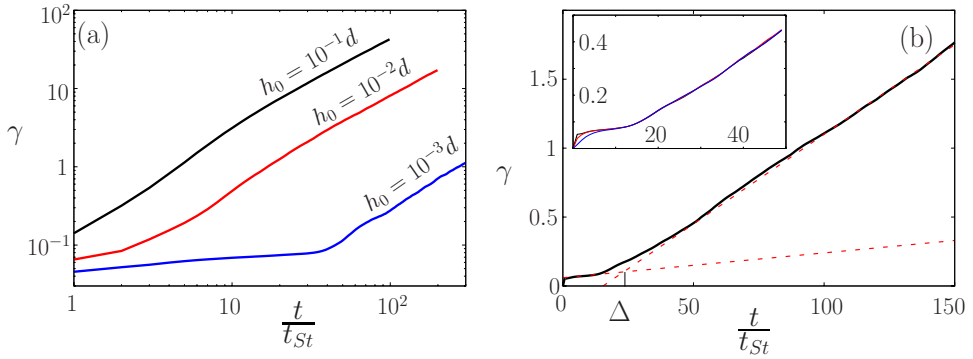

FIG. 2. (Color online) Time evolution of the shear strain γ induced by a rapid increase in shear stress σ_{xy} from 0 to $0.5\sigma_{yy}$ between $t=0$ and $t=t_{St}$. (a) Materials with a different value of the steric length h_0. (b) Procedure to determine the typical duration Δ of the creeping phase, here for $h_0/d=2\times10^{-3}$; the dashed lines correspond to the linear fit of $\gamma(t)$ in the creep phase and in the flow phase; (inset) for the same material, different rates of initial stress increase: $\beta=0.1$ (black), 0.5 (red), and 2 (blue) (see introduction of Sec. IV).

shear geometry, in the absence of gravity, with a fully periodic domain [Fig. 1(b)]. The principle of the method is detailed in Appendix B. The typical experiment consists of two steps: (i) the preparation of a dense compressed sample and (ii) the shear by itself.

First, particles are set in a loose and random configuration. They are then subjected solely to a designated target normal stress σ_{yy}. This makes the material denser, with closer particles, while the height of the periodic cell decreases. The material eventually reaches a static state where the confining stress is supported by some pairs of particles whose surface to surface distances are on the order of the steric length h_0. A correct simulation of this compression should include the long-range multibody hydrodynamics interaction, while the particles are still in a loose configuration. However, we do not focus on the compression process and use it only as a way to obtain a close-packed configuration. In the second step, which is the prime focus of our paper, we subject the configuration to a (smoothened) step in shear stress from zero to a final value σ_{xy}. We then measure the time evolution of the nominal shear strain γ. More precisely, the shear stress is continuously increased from zero to its final value within a short but finite time of the order of t_{St} [Eq. (2)] as $\sigma_{xy}(1-e^{-t/\beta t_{St}})$ (see Fig. 2). Most of the results are obtained with $\beta=1$. Different values ($\beta=0.5$ and $\beta=2$) will be used to probe the influence of the rate of the initial shear stress increase.

We perform a series of such numerical experiments for materials with various steric lengths h_0, subjected to various levels of shear stress σ_{xy}. The parameters of the system are summarized in Table II, expressed in units of particle size d for the length, normal stress σ_{yy} for the stress, and Stokes time t_{St} for the time. The grains have a mass, but we set the inertial time much smaller than the Stokes time so that the dynamics of the system is mostly driven by viscous interactions. The reduced normal stress $\kappa=\sigma_{yy}/E$ applied to the particles is much smaller than unity so that the elastic deformations would be much smaller than the particle size. We complete the current section by describing the resulting collective behavior in our soft dynamics simulations, which we will then analyze in terms of the internal dynamics in Sec. V

TABLE II. Properties of the simulated systems: inertial time t_i, reduced applied normal stress κ, steric distance h_0, and shear stress σ_{xy}.

t_i/t_{St}	$\kappa=\sigma_{yy}/E$	h_0/d	σ_{xy}/σ_{yy}
0.1	10^{-3}	$8\times10^{-4}\rightarrow10^{-1}$	$0.05\rightarrow1$

A. Role of the steric length

In the first test we subject materials with different steric lengths h_0 to a similar constant shear stress $\sigma_{xy}=0.5\sigma_{yy}$ [Fig. 2(a)]. For the longest steric distance, $h_0/d=10^{-1}$, the shear strain increases almost steadily. In contrast, for the shortest distance $h_0/d=10^{-3}$, the material first deforms very slowly. After this creep phase, it starts to flow steadily. During both the creep and the flow phases, $\gamma(t)$ is mostly linear [Fig. 2(b)]. Except for the very beginning of the creeping phase, this behavior is not sensitive to the typical time of increase in the stress [Fig. 2(b), inset]. We define the typical duration Δ of the creep phase using a geometrical construction that searches for the intersection between these two lines, as plotted in linear coordinates. Note that prior to the creep phase, there is another very short phase, during which the shear deformation quickly increases up to a small level. This corresponds to the immediate elastic deformation of the particles induced by the increase in shear stress.

Figure 3 shows the value of Δ for materials with different steric lengths h_0. The creep duration Δ naturally increases when h_0 gets smaller. However, as long as the steric length is larger than roughly $10^{-2}d$, Δ is small: only few times longer than the Stokes time. In contrast, it increases strongly for smaller h_0.

B. Varying the step shear stress

In the second test, a material with a steric length $h_0=2\times10^{-1}d$ was subjected to varying step shear stress values (Fig. 4). It appears that below a critical shear stress threshold, the material creeps and then does not seem to flow but rather reaches a static equilibrium within a finite shear strain smaller than 100%. Above this shear stress threshold, here

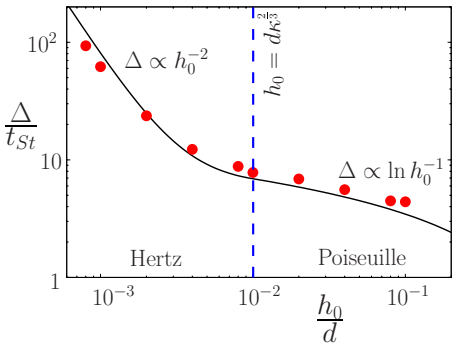

FIG. 3. (Color online) Macroscopic relaxation time Δ, estimated as shown on Fig. 2(b), as a function of the steric length h_0. Circles denote results from simulations, while the curve corresponds to three times the separation time t^{sep} for two grains as defined by Eq. (8). The third data point ($h_0/d=2\times10^{-3}$) corresponds to curve F in Fig. 4.

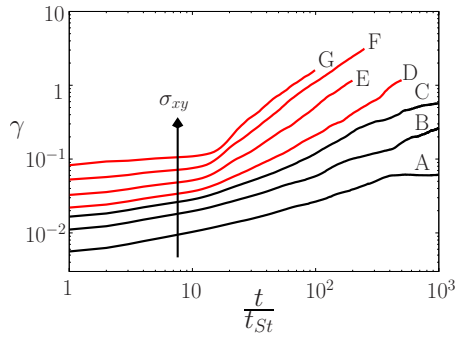

FIG. 4. (Color online) Time evolution of the shear strain γ induced by establishing (from $t=0$ to $t=t_{St}$) a constant shear stress (for larger t). Each curve corresponds to a different value of the final shear stress: (a) $\sigma_{xy}/\sigma_{yy}=0.05$, (b) 0.1, (c) 0.15, (d) 0.2, (e) 0.3, (f) 0.5, and (g) 1.0. Red (respectively, black) curves denote tests in which the material eventually flows (respectively, does not flow). The same material (with $h_0=2\times10^{-3}$) was used for each run. Curve F corresponds to one of the experiments considered in Fig. 3.

found to be roughly $\sigma_{xy}=0.2\sigma_{yy}$, the material creeps and then flows. One might imagine that the response delay in the creep phase before the onset of flow should be shorter if the applied constant shear stress is higher. Surprisingly, as can be seen from curves D–G of Fig. 4, i.e., with applied shear stresses that differ by a factor of five, it seems that the duration of the creep phase remains essentially constant although the transition from creep to flow becomes sharper for larger values of the applied shear stress.

V. MICROSCOPIC ORIGIN OF THE OBSERVED RELAXATION TIME

Let us now interpret the macroscopic behaviors observed in the previous section in terms of the dynamics of two particles in relative motion. When the material is sheared, neighboring particles need to move toward and away from each other, which includes normal approach and separation and sliding. The normal viscous friction is typically higher than the tangential one, as they are proportional to a^4/h^3 and a^2/h, respectively, and that a is larger than h in both the Poiseuille and Hertz limits [see Appendix A and Fig. 1a2]. Consequently, the normal relative motion is the slowest. As a result, most of the time the material is situated where interparticle contacts can be viewed as frictionless as far as sliding is concerned, with only normal forces acting to bring particles into contact or away from each other in a slow motion. Hence, we focus on the sole normal mode for interpreting the macroscopic observations.

The duration of the normal separation process depends on the initial distance between surfaces, on the viscous friction, and on the typical force transmitted by the fluid in the gap. The typical initial distance between the surfaces can be estimated as the steric distance h_0. As the step in shear stress is applied to the dense material, the initial viscous friction depends on whether the interaction is initially in the Poiseuille regime ($\delta<h_0$) or in the Hertz limit ($\delta>h_0$). Initially, the typical force transmitted within a pair of particles scales with $\sigma_{yy}d^2$. Hence, the interaction lies in the Hertz limit when $h_0/d<\kappa^{2/3}$ ($\kappa=\sigma_{yy}/E$).

Let us assume that, when the shear stress is applied, the typical transmitted force is still of the order of $\sigma_{yy}d^2$. Then, the time t^{sep} for two particles to separate is such that $\int_{t=0}^{t^{sep}}\sigma_{yy}d^2dt=\int_{h=h_0}^{h_{sep}}\frac{3}{2}\pi\eta\frac{a^4}{h^3}dh$, where the dimension of the force-transmitting region is $a=\sqrt{dh}$ in the Poiseuille limit and $a=\sqrt{d|\delta|}$ in the Hertz limit. Hence

$$\frac{t^{sep}}{t_{St}}=\begin{cases}\frac{1}{2}\ln\left(\frac{h_{sep}}{h_0}\right) & \left(\text{Poiseuille},\ \frac{h_0}{d}\gg\kappa^{2/3}\right)\\ \frac{1}{4}\left[\kappa^{4/3}\left(\frac{d}{h_0}\right)^2-1\right]+\frac{1}{2}\ln\left(\frac{h_{sep}}{d\kappa^{2/3}}\right) & \left(\text{Hertz},\ \frac{h_0}{d}\ll\kappa^{2/3}\right).\end{cases} \tag{8}$$

An arbitrary value of h^{sep} has to be defined at the end of the separation process. Basically, it should be of the order of d. But the time of separation is only slightly depending on it. In the Poiseuille limit, the time of separation is at the order of the stokes time, with almost no effect by the small steric length h_0. In the Hertz limit, in contrast, it is strongly dependent on h_0 as well as on the reduced normal stress $\kappa=\frac{\sigma_{yy}}{E}$. When applied to the system simulated in the previous section

($\kappa=10^{-3}$), this simple separation time t^{sep} captures the scaling behavior of the creep time Δ (Fig. 3). The data are quantitatively well represented by the function bt^{sep} involving a fit parameter $b\approx 3$. This constant is likely to rely on the details of the contact network (number of coordination, heterogeneities, anisotropy,…) and may also slightly depend on the geometrical definition of Δ [Fig. 2(b)]. The salient result is that, surprisingly enough, this very simple model with only one interaction and a single force scale $\sigma_{yy}d^2$ captures the macroscopic delay observed: both t^{sep} and Δ scales with $\ln h_0^{-1}$ while the interaction is initially in the Poiseuille regime ($h_0 > \kappa^{2/3}=10^{-2}$), and with h_0^{-2} if the interaction is initially in the Hertz regime (see Fig. 3).

However, this model does not account for the secondary effect of the shear stress we observed in Fig. 4. Basically, one could expect that under a larger applied shear stress, the typical tensile pairwise normal force would increase. Accordingly, one should observe a shorter separation time. Figure 4 reveals that the creeping time appears to be essentially independent of the applied shear stress. This may have some connection although probably not direct, with the counterintuitive effect highlighted in [27] concerning the crossover between the Poiseuille and the Hertz regimes: there exists an optimal tensile force that minimizes the time of separation between two particles. This optimal force corresponds to the transition between the Hertz and the Poiseuille regimes. Thus, it depends on the gap h as: $F^{opt}\approx Ed^2(\frac{h}{d})^{3/2}$ (see [27] for more details). Increasing the force then brings the system further into the Hertz regime, which strongly increases the viscous friction and eventually results in a slower separation.

VI. DISCUSSION

The separation dynamics between two grains appears to collectively generate the observed delay of the static-to-flow transition. This is supported by the evolution of the gap distribution during this process, shown in Fig. 5. The gap distribution is initially concentrated around h_0. When the flow establishes, it evolves toward a steady distribution which is more developed toward larger gaps. This final state is quickly reached in materials at the Poiseuille limit [Fig. 5(a)]. By contrast, in materials at the Hertz limit, the evolution is slow: its duration is typically that of the creeping phase, during which gaps globally widen, even though some of them get closer at first [see Fig. 5(b)].

Finally, Fig. 6 shows that the static-to-flow transition is associated with a dilatancy effect, as already observed in various studies (see, for instance, [20,21]). The dilatancy is rather small during the creeping phase, and becomes more significant only around the onset of flow. Hence, the pore pressure should not play a significant role during the creeping phase. Instead, this phase relies on the local dynamics of the grain surface separation. In the present case, when the material is ready to dilate because the relevant gaps are widened, the pore pressure could lead to a second delay. A similar effect may be expected from the dynamical competition between the formation and breakage of hydrodynamic clusters [49].

Further studies of the steady flow regime should provide new insights on a major issue in suspension flows: viscosity

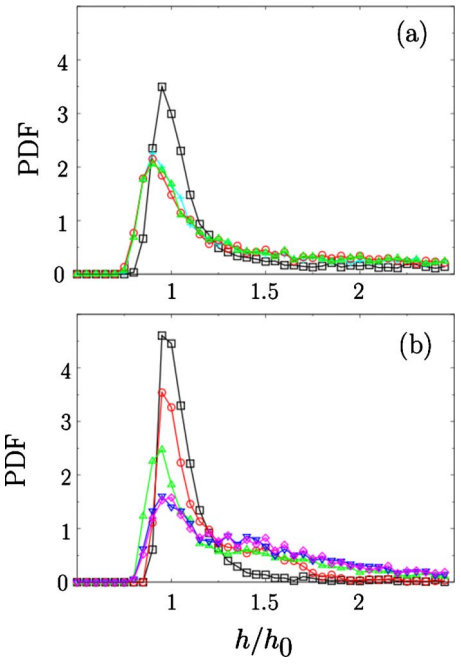

FIG. 5. (Color online) Gap probability density function (PDF) at different times during the static-to-flow transition induced by a smoothed step of shear stress $\sigma_{xy}=0.5\sigma_{yy}$ at $t=0$. Materials with steric length (a) $h_0/d=10^{-1}$ and (b) 10^{-3}; time $t/t_{St}=0$ (□), 5(+), 10 (○), 100 (△), 200 (▽), and 300 (◇). It appears that the gap distribution evolves more slowly in the Hertz limit, illustrating the connection between the microstructure and the macroscopic delay.

is usually expressed as a function of the solid fraction for dilute suspensions, but when grains becomes denser, models fail to describe experimental data [7,50–52]. The results presented in the current paper show that the solid fraction in the steady regime fluctuates around a steady value which depends on the steric length h_0 (Fig. 6, inset). Meanwhile, Fig.

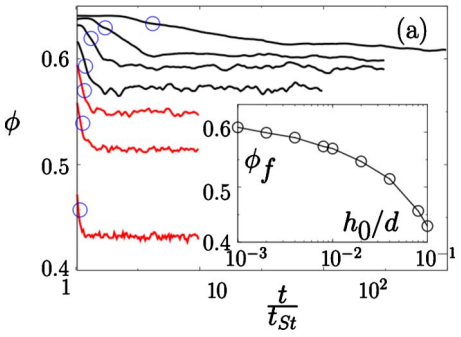

FIG. 6. (Color online) Dilatancy during the static-to-flow transition induced by a smoothed step of shear stress $\sigma_{xy}=0.5\sigma_{yy}$ at $t=0$: solid fraction ϕ (ratio of the volume of the grains by the volume of the cell) as a function of time, for materials with different steric length h_0 (curves from the bottom to the top correspond to $h_0/d=10^{-1}$, 4×10^{-2}, 2×10^{-2}, 10^{-2}, 4×10^{-3}, 2×10^{-3}, and 10^{-3}); circles are placed on these curves at the time corresponding to the macroscopic delay shown in Fig. 3; (inset) solid fraction ϕ_f in the steady flow regime as a function of the steric length h_0: each point corresponds to the asymptotic value of the solid fraction $\phi(t)$ shown in the main plot.

2(a) shows that the steady shear rate is the same for those materials. This indicates that there is no unique relationship between the effective viscosity and the solid fraction, and that other parameters that account for the detail of the interaction should be involved.

VII. CONCLUSION

The distinction between the flowing and nonflowing states of many materials is critical for determining failure. The current paper focuses on studying the micromechanical origins of this phenomenon in relation to ideal materials of closed-packed elastic particles in a viscous fluid. Using soft dynamics simulations, we show that when subjected to a step shear stress, this material can exhibit a long creep phase before a steady flow state sets in. The typical creep time seems to rely on an internal relaxation process, namely, the normal separation of two particles, which is driven by the applied stress and resisted by the viscous friction. This internal relaxation time thus depends on (i) the applied stress, (ii) the particle stiffness, and (iii) the steric length h_0 below which particle surfaces interact directly.

The direct surface-to-surface interaction enables the material to statically sustain a confining stress, and whether or not the steric length is shorter than the typical elastic deflection strongly affects the scaling behavior of the viscous friction. On the one hand, the relaxation time is not very long in the Poiseuille regime (large h_0 and/or very stiff particles) as its scales with $\ln(h_0^{-1})$ and is thus only slightly longer than the Stokes time. On the other hand, the relaxation time can be very long in the Hertz limit (small h_0 and/or soft particles) as it then scales with h_0^{-2} (see the estimation in Table I).

The long aging process corresponding to the Hertz limit should be a common characteristic of various immersed particulate materials like granular pastes, emulsions and foams. We expect that the soft bubbles and droplets would reach the Hertz regime for relatively low confining stresses. For the solid grains, a rough estimate can be performed according to Hertz's elasticity which defines the Hertz limit for $h_0 < d(\frac{\sigma_{yy}}{E})^{2/3}$. Assuming that the steric length h_0 is determined by a surface roughness of amplitude 0.1 μm, that the grain size is $d \simeq 1$ mm, and that their Young modulus is $E \simeq 10^{10}$ Pa, then the normal stress required to reach the Hertz regime would be on the order of $\sigma_{yy} \simeq 10^4$ Pa. Note, however, that these materials involve further modes of interaction such as solid friction, interfacial rheology, and adhesion, which would (i) induce other time scales and (ii) affect the hydrodynamics within the gap and thus the expression of the viscous friction which the aging process relies on. In future works, we hope to include some such detailed interactions within our methodology.

ACKNOWLEDGMENTS

Financial supports for this research from the Australian Government's Flagship Collaboration Fund through the CSIRO Flagship Cluster on Subsea Pipelines and from the French Government through the Agence Nationale de la Recherche (Grant No. ANR-05-BLAN-0105-01) are appreciated.

APPENDIX A: LUBRICATION BETWEEN ELASTIC SURFACES

The viscous flow between two close elastic spheres is not a simple problem. However, simple scaling formulas can be deduced considering that only a small portion of the surface transmits the force (size a) and that its radius of curvature is large ($a \ll R$). Then, the hydrodynamical interaction is similar to that which develops between two flat parallel disks of radius a separated by h. The low aspect ratio of the gap, $\frac{h}{a} \ll 1$ favors flows in the Stokes regime.

A simple way to get the scaling formulas for the viscous force and torque is to consider the average shear strain rate $\dot{\epsilon}$ in the liquid, which scales like $\frac{v^s}{h}$ for a Couette flow and like $\frac{3}{2}\frac{v^s}{h}\frac{\pi a^2}{2\pi a h}$ for a Poiseuille flow. On the one hand, the power dissipated by the viscous flow in a gap of a volume $\pi a^2 h$ scales with $\eta \dot{\epsilon}^2 a^2 h$. On the other hand, this power is equal to $F^{vis} v^s$ for a relative velocity v^s and to $\Gamma^{vis} w^s$ for a relative angular velocity w^s. This leads to the expressions of the viscous forces and torques in Fig. 7. Note that the viscous force and torque can be expressed through the viscous friction tensors Z and w:

$$\vec{F}^{vis} = Z \cdot \vec{v}^s, \quad \text{with} \quad Z = \zeta \vec{n} \otimes \vec{n} + \lambda (I - \vec{n} \otimes \vec{n}),$$

$$\vec{\Gamma}^{vis} = W \cdot \vec{w}^s, \quad \text{with} \quad W = a^2 Z, \tag{A1}$$

where $\vec{n}$ is the unit vector normal to the surface, I is the unity tensor, and $\otimes$ is the standard cross product.

The elastic forces and torques can also be estimated in a simple way by following the Hertz theory: the elastic strain ϵ concerns mostly a small region of volume a^3. It scales according to $\frac{\delta}{a}$ for both the normal and the tangential deflections represented by δ, and as $\frac{a\theta}{a}$ for a twist angle θ. The total elastic energy, $E\epsilon^2$, therefore scales like $Ea^3(\frac{\delta}{a})^2$ for deflections and according to $Ea^3\theta^2$ for twists. The differentiation of these energies with respect to δ and θ gives the scaling for the elastic forces and torques expressed in Fig. 7, where all numerical constants are set to unity for the sake of simplicity.

APPENDIX B: SOFT DYNAMICS METHOD

We have developed the soft dynamics method to simulate large samples of closely packed particles with elastolubricated interaction [27,28]. In the present work, the particles are inertial so that their motion is deduced from the forces and torques they experience according to Newton's law, as in the standard discrete element methods:

$$\begin{cases} m_i \ddot{\vec{X}}_i = \vec{F}_i^{ext} + \sum_j \vec{F}_{ij}^{ela} \\ J_i \dot{\vec{\Omega}}_i = \vec{\Gamma}_i^{ext} + \sum_j \{\vec{\Gamma}_{ij}^{ela} + \vec{r}_{ij} \times \vec{F}_{ij}^{ela}\}, \end{cases} \tag{B1}$$

where m_i and J_i are, respectively, the mass and the inertia moment of particle i, $\vec{X}_i$, and $\vec{\Omega}_i$ its position and its rotation

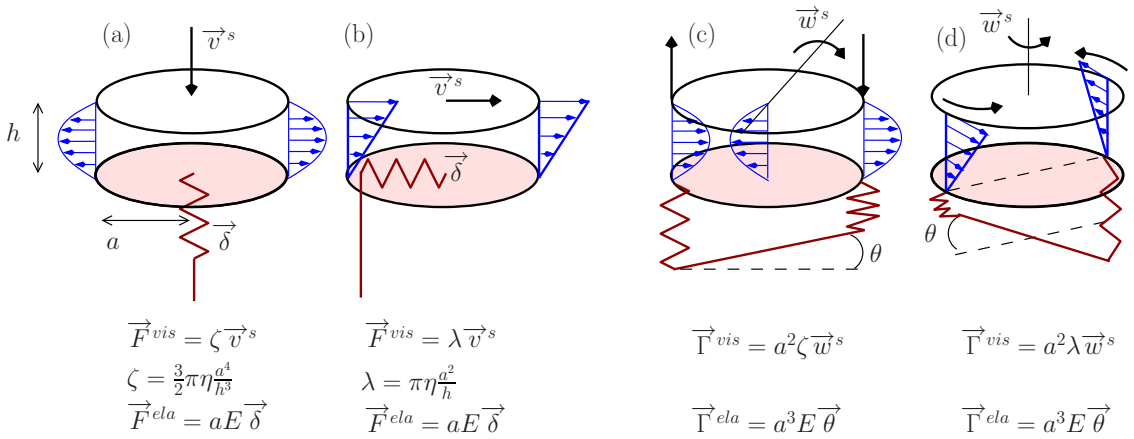

FIG. 7. (Color online) Scheme of the elastohydrodynamical interaction implemented in soft dynamics, including four modes of relative motion between particles with a surface-to-surface distance of h. Distance a is the size of the transmitting force region [see Fig. 1(a)]. The blue arrows designate the flow velocity profile and the red spring the elastic deformation of the bulk material. The corresponding expressions of viscous and elastic forces or torques are as follows. (a) The normal approach induces a Poiseuille flow and an associated viscous friction ζ (also valid for a normal separation). (b) The tangential sliding induces a Couette flow and an associated viscous friction λ. (c) Normal rotation (locally, the flow is like a Poiseuille flow). (d) Parallel rotation (locally, the flow is like a Couette flow).

velocity. $\vec{F}_i^{ext}$ and $\vec{\Gamma}_i^{ext}$ are possible external force and torque that the particle experiences, which are both taken as zero in the present study. The sums run on each particle j interacting with i. The force $\vec{F}_{ij}^{ela}$ and the torque $\vec{\Gamma}_{ij}^{ela}$ come from the elastic deflection and twist of the particle surfaces, and $\vec{r}_{ij}$ is the vector from the center of i to the interaction point.

The uniqueness of the soft dynamics approach is to include the dynamics of the elastic deflection $\vec{\delta}_{ij}$ and twist angle $\vec{\theta}_{ij}$ so that the force and torque balances are satisfied for each interaction. $\dot{\vec{\delta}}_{ij}$ and $\dot{\vec{\theta}}_{ij}$ can be deduced from the difference between the particle velocities, $\dot{\vec{X}}_i$ and $\vec{\Omega}_i$, and the relative translational and rotational velocities of particle surfaces, $\vec{v}_{ij}^s$ and $\vec{w}_{ij}^s$. Compatibility then requires having

$$\begin{cases} \dot{\vec{\delta}}_{ij} = \dot{\vec{X}}_j + \dot{\vec{\Omega}}_j \times \vec{r}_{ji} - [\dot{\vec{X}}_i + \dot{\vec{\Omega}}_i \times \vec{r}_{ij}] - \vec{v}_{ij}^s \\ \dot{\vec{\theta}}_{ij} = \dot{\vec{\Omega}}_j - \dot{\vec{\Omega}}_i - \vec{w}_{ij}^s. \end{cases} \tag{B2}$$

For each of the interactions, the relative velocities $\vec{v}_{ij}^s$ and $\vec{w}_{ij}^s$ are given by the force or torque balances:

$$\begin{cases} \vec{F}_{ij}^{ela} = \vec{F}_{ij}^{vis} + \vec{F}_{ij}^{dir} \\ \vec{\Gamma}_{ij}^{ela} = \vec{\Gamma}_{ij}^{vis} + \vec{\Gamma}_{ij}^{dir}, \end{cases} \tag{B3}$$

and the fact that the viscous force or torque are proportional to them through the friction tensors Z_{ij} and W_{ij} (see Appendix A):

$$\begin{cases} \vec{v}_{ij}^s = Z_{ij}^{-1} \cdot [\vec{F}_{ij}^{ela} - \vec{F}_{ij}^{dir}] \\ \vec{w}_{ij}^s = W_{ij}^{-1} \cdot [\vec{\Gamma}_{ij}^{ela} - \vec{\Gamma}_{ij}^{dir}]. \end{cases} \tag{B4}$$

The second order Eqs. (B2) are integrated using a standard predictor-corrector scheme, while the first order Eqs. (B3) are integrated using a simple Euler scheme. The time step of integration is a fraction of the shortest time scale in the system, namely $t_M = \frac{\eta}{E}$. Through careful examination we found that a time step of five time smaller than t_M is short enough.

Since we do not include long-range hydrodynamical interactions, it is sensible to introduce a cut-off distance: here two particle interact only if their surface to surface distance is smaller than $0.25d$. The size of the transmitting force region a is then being interpolated between the two asymptotic limits of the Poiseuille and the Hertz models, as a way to get a continuous transition. The interpolation we choose is: $a = \sqrt{d(h+|\delta|)}$. Note that different choices of interpolation are possible although this should have no incidence except in the vicinity of the crossover between both scaling regimes.

[1] R. Höhler and S. Cohen-Addad, J. Phys.: Condens. Matter **17**, R1041 (2005).
[2] N. Denkov, S. Tcholakova, K. Golemanov, K. Ananthpadmanabhan, and A. Lips, Soft Matter **5**, 3389 (2009).
[3] L. Bécu, S. Manneville, and A. Colin, Phys. Rev. Lett. **96**, 138302 (2006).
[4] S. Derkach, Adv. Colloid Interface Sci. **151**, 1 (2009).
[5] L. Bocquet, A. Colin, and A. Ajdari, Phys. Rev. Lett. **103**, 036001 (2009).
[6] F. Yilmaz and M. Gundogdu, Korea-Aust. Rheol. J. **20**, 197 (2008).
[7] J. Stickel and R. Powell, Annu. Rev. Fluid Mech. **37**, 129

(2005).
[8] P. Coussot, *Rheometry of Pastes, Suspensions, and Granular Materials* (Wiley-Interscience, New York, 2005).
[9] P. Sollich, F. Lequeux, P. Hébraud, and M. Cates, Phys. Rev. Lett. **78**, 2020 (1997).
[10] P. Richard, M. Nicodemi, R. Delannay, P. Ribiere, and D. Bideau, Nature Mater. **4**, 121 (2005).
[11] G. Marty and O. Dauchot, Phys. Rev. Lett. **94**, 015701 (2005).
[12] P. Coussot, Soft Matter **3**, 528 (2007).
[13] H. Barnes, J. Non-Newtonian Fluid Mech. **70**, 1 (1997).
[14] F. Da Cruz, F. Chevoir, D. Bonn, and P. Coussot, Phys. Rev. E **66**, 051305 (2002).
[15] P. C. F. Møller, J. Mewis, and D. Bonn, Soft Matter **2**, 274 (2006).
[16] A. Grillet, R. Rao, D. Adolf, S. Kawaguchi, and L. Mondy, J. Rheol. **53**, 169 (2009).
[17] T. Narumi, H. See, A. Suzuki, and T. Hasegawa, J. Rheol. **49**, 71 (2005).
[18] H. M. Wyss, K. Miyazaki, J. Mattsson, Z. Hu, D. R. Reichman, and D. Weitz, Phys. Rev. Lett. **98**, 238303 (2007).
[19] R. Iverson, Journal of Geophysical Research **110**, F02015 (2005).
[20] M. Pailha, M. Nicolas, and O. Pouliquen, Phys. Fluids **20**, 111701 (2008).
[21] S. Marze, A. Saint-Jalmes, and D. Langevin, Colloids Surf., A **263**, 121 (2005).
[22] G. K. Batchelor, *An Introduction to Fluid Dynamics* (Cambridge University Press, Cambridge, 1967).
[23] G. Bossis and J. F. Brady, J. Chem. Phys. **80**, 5141 (1984).
[24] J. F. Brady and G. Bossis, Annu. Rev. Fluid Mech. **20**, 111 (1988).
[25] M. L. Ekiel-Jeżewska, T. Gubiec, and P. Szymczak, Phys. Fluids **20**, 063102 (2008).
[26] S. Faure, S. Martin, B. Maury, and T. Takahashi, in *ESAIM: Proceedings* (EDP Sciences, 2009), Vol. 28, pp. 55–79. 10.1051/proc/2009039
[27] P. Rognon and C. Gay, Eur. Phys. J. E **27**, 253 (2008).
[28] P. Rognon and C. Gay, Eur. Phys. J. E **30**, 291 (2009).
[29] J. Jenkins and M. Koenders, Granular Matter **7**, 13 (2005).
[30] O. I. Vinogradova and G. E. Yakubov, Phys. Rev. E **73**, 045302(R) (2006).
[31] L. Yang, J. Seddon, T. Mullin, C. Del Pino, and J. Ashmore, J. Fluid Mech. **557**, 337 (2006).
[32] T. Divoux and J. C. Geminard, Phys. Rev. Lett. **99**, 258301 (2007).
[33] Martin-D. Lacasse, G. S. Grest, and D. Levine, Phys. Rev. E **54**, 5436 (1996).
[34] M. Durand and H. A. Stone, Phys. Rev. Lett. **97**, 226101 (2006).
[35] L. M. C. Sagis, Phys. Rev. Lett. **98**, 066105 (2007).
[36] S. Tabakova and K. Danov, J. Colloid Interface Sci. **336**, 273 (2009).
[37] S. Besson, G. Debregeas, S. Cohen-Addad, and R. Höhler, Phys. Rev. Lett. **101**, 214504 (2008).
[38] N. D. Denkov, S. Tcholakova, K. Golemanov, and A. Lips, Phys. Rev. Lett. **103**, 118302 (2009).
[39] F. da Cruz, F. Lechenault, and O. Dauchot, in *Powders and Grains 2005*, edited by R. Garcia-Rojo, H. J. Herrmann, and S. McNamara (A.A. Balkema, Leiden, The Netherlands, 2005), pp. 7–11.
[40] GDR MiDi, Eur. Phys. J. E **14**, 341 (2004).
[41] Y. Forterre and O. Pouliquen, Annu. Rev. Fluid Mech. **40**, 1 (2008).
[42] C. Cassar, M. Nicolas, and O. Pouliquen, Phys. Fluids **17**, 103301 (2005).
[43] D. Doppler, P. Gondret, T. Loiseleux, S. Meyer, and M. Rabaud, J. Fluid Mech. **577**, 161 (2007).
[44] A. Lemaître, J.-N. Roux, and F. Chevoir, Rheol. Acta **48**, 925 (2009).
[45] C. Campbell, J. Fluid Mech. **539**, 273 (2005).
[46] D. J. Durian, Phys. Rev. Lett. **75**, 4780 (1995).
[47] D. J. Durian, Phys. Rev. E **55**, 1739 (1997).
[48] A. W. Lees and S. Edwards, J. Phys. C **5**, 1921 (1972).
[49] P. Mills and P. Snabre, Eur. Phys. J. E **30**, 309 (2009).
[50] G. Ovarlez, F. Bertrand, and S. Rodts, J. Rheol. **50**, 259 (2006).
[51] N. Huang and D. Bonn, J. Fluid Mech. **590**, 497 (2007).
[52] C. Bonnoit, T. Darnige, E. Clement, and A. Lindner, J. Rheol. **54**, 65 (2010).